Spin wave instability in single crystal Zn–Y hexagonal ferrite at 8.93 GHz

Richard G. Cox,[a] Carl E. Patton, Michael A. Wittenauer, Pavel Kabos, and Liang Chen
Department of Physics, Colorado State University, Fort Collins, Colorado 80523

(Received 5 October 2000; accepted for publication 7 January 2001)

Resonance saturation (RS), subsidiary absorption (SA), and parallel pump (PP) spin wave instability threshold measurements have been made on single crystal easy plane disks of Mn substituted Zn–Y type hexagonal ferrite materials at 8.93 GHz and room temperature. For each configuration, ''butterfly curves'' of the spin wave instability threshold microwave field amplitude h_{crit} as a function of the static field applied in the disk plane were obtained. The previous theory for these instability processes was also extended to include planar magnetocrystalline anisotropy and a wave vector **k** dependent spin wave linewidth, ΔH_k. The RS butterfly curve had a characteristic ''V'' shape with a rounded minimum at the ferromagnetic resonance (FMR) field. The nominal ΔH_k needed to fit the data at the ferromagnetic resonance field was 7 Oe, but the butterfly curve shape indicated a **k**-dependent ΔH_k. The butterfly curves for the PP configuration were flat at low field and then diverged rapidly at the cutoff field for first order instability processes, H_{cut}. The SA butterfly curves were also flat over the field interval for first order processes, but then decreased as the field was increased above H_{cut}. This decrease is attributed to the onset of second order processes due to the proximity of the FMR and additional magnetostatic mode peaks as one moves to and then above H_{cut}. The flat portions of the PP and SA butterfly curves could be fitted with a single **k**-independent ΔH_k value of 18 Oe. © *2001 American Institute of Physics.*
[DOI: 10.1063/1.1352689]

I. INTRODUCTION

Microwave ferrite devices have unique properties for radar applications and there is a critical need for such devices in the millimeter wave frequency regime. The main problem with the use of conventional cubic ferrites in millimeter wave devices is the need for large external magnetic fields. At 60 GHz, for example, the required fields are in the 20 kOe range. The large uniaxial or planar magnetocrystalline anisotropy in hexagonal ferrite materials offers a possible solution to this problem.[1–3] Typical anisotropy fields are in the 10–20 kOe range. Such large effective fields can result in a substantial reduction in the biasing field requirements for millimeter wave devices.

Wittenauer *et al.*[4] have reported on the growth of uniaxial Ba–M ($BaFe_{12}O_{19}$) hexagonal ferrite materials for use at millimeter wave frequencies. The same group has used a similar technique, based on the earlier work of Savage *et al.*,[5] to produce Zn–Y ($Ba_2Zn_2Fe_{12}O_{22}$) materials with easy plane anisotropy. Easy plane anisotropy may be preferable for latching device applications because of the reduced energy required for switching between different remanent states.[6,7] However, many problems remain for the actual device implementation of easy plane hexagonal ferrite materials in millimeter wave devices. Two such problems concern the low power losses and the high power response. The low power loss problems generally involve microstructural defects and inhomogeneities.[8,9] The high power response problem involves the onset of nonlinear effects that translate into practical power limits for real devices. These nonlinear effects are due to the parametric generation of spin waves and are generically called spin wave instability processes.[10]

This work is concerned with the high power microwave properties of single crystal Zn–Y hexagonal ferrite materials. The approach was to measure the microwave field amplitude required for the onset of spin wave instability as a function of the static magnetic field H_{ext}. Plots of the threshold microwave field amplitude h_{crit} vs. H_{ext} are termed ''butterfly curves.'' Such curves yield immediate information on the power limits of the ferrite because the measured h_{crit} thresholds can be readily converted to power levels for specific device configurations. The butterfly curve data were analyzed with a modified version of the spin wave instability theory originally developed by Suhl[11] and Schlömann.[12] Such an analysis provides information on: (i) the critical spin wave modes which are generated at the nonlinear threshold and (ii) the spin wave linewidth ΔH_k, which is the relaxation rate of the critical spin wave modes expressed in linewidth units. Both items are important for the optimization of millimeter wave ferrite devices and for further materials development to produce low loss hexagonal ferrites.

There were three main objectives for this work: (i) to measure spin wave instability thresholds for a range of static magnetic fields and microwave pump field configurations; (ii) to use these data to construct resonance saturation, subsidiary absorption, and parallel pump butterfly curves; (iii) to analyze the butterfly curves and determine the critical spin wave modes which are excited at threshold and the spin wave linewidths associated with these modes. The results presented here constitute the first extensive work on butterfly curves for planar hexagonal ferrites in all three pumping configurations.

[a]Electronic mail: richcox@lamar.colostate.edu

 © 2001 American Institute of Physics

Downloaded 02 Apr 2001 to 129.82.192.18. Redistribution subject to AIP copyright, see http://ojps.aip.org/japo/japcr.jsp

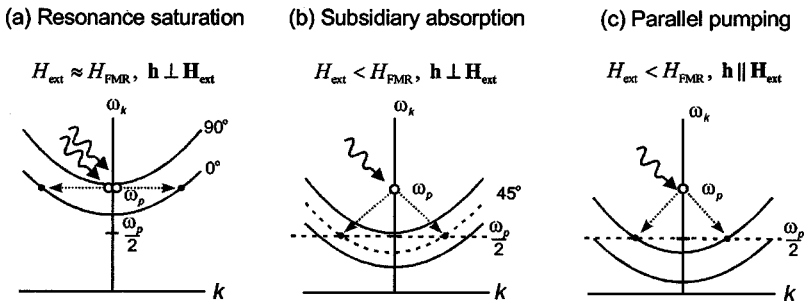

FIG. 1. (a), (b), and (c) show schematic spin wave bands of the spin wave frequency ω_k vs. wave number k for resonance saturation, subsidiary absorption, and parallel pumping, respectively. Allowed modes lie between the solid 0° and 90° curves in each diagram. The degree values indicate the polar propagation angle for spin waves and the diagrams are for an isotropic material. For (a), the external field H_{ext} is close to the ferromagnetic resonance field H_{FMR}. The **h** term denotes the microwave field. (○) indicate uniform mode magnons at ω_p. (●) indicate the critical spin wave modes at ω_p in (a) and at $\omega_p/2$ in (b) and (c). The wavy arrows indicate the microwave photon.

The organization of the article is as follows: Sec. II reviews the resonance saturation, subsidiary absorption, and parallel pumping spin wave instability processes. The section covers the experimental effects, the theory, and the procedure for the critical mode and threshold analysis. Section III presents details on the materials, the measurement techniques, and the microwave field configuration and calibration. Section IV gives the experimental results and a brief analysis. Section V provides a summary and conclusion.

II. SPIN WAVE INSTABILITY

A. Microwave response at high power

As already indicated, the observed nonlinear microwave response of ferrites at high power is due to the parametric excitation of spin waves. This excitation process can be separated into three steps. First, microwave energy is coupled into the available spin wave modes either indirectly through the uniform mode response or directly through the microwave field. Second, the excited spin waves lose this energy through normal relaxation processes. Third, at the point in input power at which the rate of energy flow into a given spin wave compensates the decay, that mode may be excited above thermal levels. The particular mode that satisfies this condition at the lowest power is referred to as the critical mode. The experimental signature of this instability is an abrupt change in the microwave loss as one exceeds the threshold power.

Instability processes may be classified into three categories, resonance saturation (RS), subsidiary absorption (SA), and parallel pumping (PP).[12] Resonance saturation occurs for static fields near the ferromagnetic resonance field (FMR) field. It is driven by the component of the microwave field that is transverse to the saturation magnetization direction, the same component which excites the FMR response at low power. For this process, the pump field excites spin waves indirectly through the dynamic magnetization associated with the uniform mode FMR response at the pump frequency ω_p. Subsidiary absorption is also driven by the uniform mode. In this case, however, the uniform mode couples to spin waves at one half the pump frequency. The range of static fields for which the coupling is strongest is generally below the range of fields for the FMR peak response. Hence, the term ''subsidiary absorption'' is used. Parallel pumping is similar to subsidiary absorption in that the coupling is to spin waves at $\omega_p/2$. The coupling here, however, occurs directly through the component of the microwave field which is parallel to the static field and the static magnetization. The range of static fields for parallel pumping is the same as for subsidiary absorption. The acronyms RS, SA, and PP will be used below for reference to these processes.

Figure 1 shows the three processes in a simplified diagrammatic form. The three illustrations show spin wave band diagrams of frequency ω_k versus wave number k for isotropic ferrites and the three configurations of interest, as indicated. The nomenclature is given in the caption. The spin wave band consists of the region between the 0° lower bound and 90° upper bound curves in each diagram. These are the limiting values of the polar spin wave propagation angle θ_k for the spin wave wave vector **k**. The wave vector nomenclature will be discussed in Sec. II C.

Quantitative remarks on the actual theory will be given in Sec. II B. The main point of the diagrams in Fig. 1 is to give a physical overview of the interactions and the critical modes for the three processes. For resonance saturation, the spin wave band limits at $k \approx 0$ are in the same range as the pump frequency ω_p. Here, two microwave pump field photons excite two uniform mode or $k \approx 0$ magnons at ω_p. These uniform mode magnons then combine to create two oppositely directed magnons at $\omega_k = \omega_p$, $\theta_k = 0$, and nonzero **k**. This is a second order process because two input uniform mode magnons are involved. In the classical theory, this corresponds to a coupling that scales with the square of the transverse component of the microwave field **h**. This transverse component will be denoted as h_t.

For the subsidiary absorption and parallel pumping processes, one microwave photon creates two magnons at $\omega_k = \omega_p/2$ with opposite **k** values. This occurs indirectly through a $k \approx 0$ magnon for the subsidiary absorption process and directly for the parallel pumping process. If the static field is above some cutoff value H_{cut}, there will be no $\omega_k = \omega_p/2$ magnons available within the spin wave band and these processes are disallowed. For subsidiary absorption, the strongest coupling is for magnons close to $\theta_k = 45°$. For parallel pumping, the coupling is strongest for $\theta_k = 90°$. The two processes are first order since only one incident photon

Downloaded 02 Apr 2001 to 129.82.192.18. Redistribution subject to AIP copyright, see http://ojps.aip.org/japo/japcr.jsp

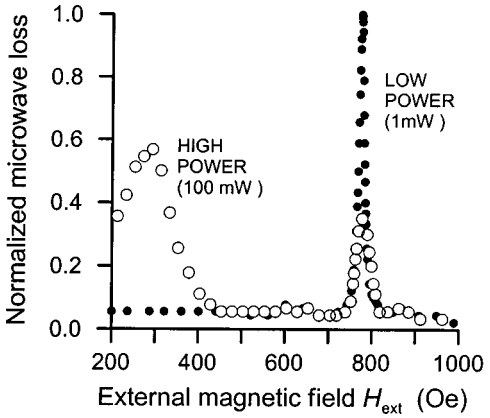

FIG. 2. Microwave loss vs static magnetic field for a 0.09 mm thick Mn substituted Zn–Y easy plane disk at low and high power, as indicated. The frequency was 8.93 GHz. The static field was in the disk plane. The linearly polarized microwave field was in plane and at an angle of 8° with the static field.

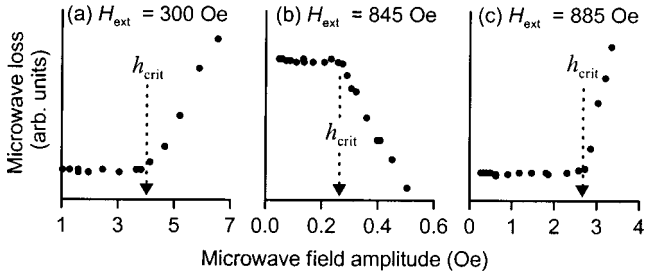

FIG. 3. Microwave loss vs microwave field amplitude for a 0.12 mm thick Mn substituted Zn–Y easy plane disk at 8.93 GHz; (a) is for parallel pumping; (b) and (c) are for resonance saturation. The static field H_{ext} was in the disk plane and at the values indicated. For (b) and (c), the microwave field was in-plane and at and angle of 8° with H_{ext}. The field axes show the transverse component only. The arrows indicate microwave field values at the spin wave instability threshold points, h_{crit}.

or magnon is involved. In the classical analysis, this corresponds to a coupling that scales linearly with the microwave field amplitude h.

The spin wave modes indicated by the solid circles in the diagrams in Fig. 1 represent the critical modes responsible for the observed instability effects. The calculation of these lowest threshold modes as a function of the static field and pumping configuration is the main function of the analysis in the next section. Once determined, the measured threshold microwave field amplitude h_{crit} allows one to obtain the spin wave linewidth ΔH_k. One may also assume various $\Delta H_k(\mathbf{k})$ functions and fit theoretical butterfly curves to the data.

As noted above, the onset of a given process is observed as a rapid change in the absorbed microwave power as the power is increased above the threshold level. Consider resonance saturation as an example. In the usual low power ferromagnetic resonance experiment, one typically observes a relatively sharp and narrow absorption line centered about the FMR field. However, when the same measurement is performed at high power, two new effects are observed: (i) there is a decrease in the peak response accompanied by a broadening of the absorption line, and (ii) there is an increase in the losses over a range of magnetic fields which is typically well below ferromagnetic resonance.[13,14]

Figure 2 shows Zn–Y microwave loss versus static magnetic field data, measured as part of this study, which demonstrate these effects. As indicated, the solid and open circles show the response at low and high power levels. The vertical axis shows absorbed microwave power on a scale which is normalized to the maximum absorption at the FMR peak. The data are for a relatively thin single crystal Zn–Y hexagonal ferrite easy plane disk with the static field in the disk plane. The microwave magnetic field was linearly polarized in the disk plane and oriented at an 8° angle to the static field direction. The microwave frequency was 8.93 GHz. The particular disk used for these data was one of three samples that were used for the full slate of measurements and analysis to be considered in Secs. IV and V.

The effect of high power on the FMR response and the low field loss region is clearly evident from Fig. 2. For the FMR absorption line, the amplitude of the peak response drops and the linewidth increases by factors of about 2.5. For fields between 200 and 400 Oe, there is a substantial increase in the losses. This field region will be termed the subsidiary loss region throughout the rest of this article. Both effects are related to the parametric excitation of spin waves. As noted above, these are also threshold effects. That is, for a given static field, the change from the low to high power response takes place abruptly at a specific threshold power level. For incident power levels below this threshold, the sample loss scales linearly with the incident power. Above threshold, the response is highly nonlinear. The change in the loss at threshold can consist of an increase or a decrease, depending on the setting of the static field.

Resonance saturation is the origin of the broadened FMR response in Fig. 2. Subsidiary absorption and parallel pumping are the origin of the broad loss region at static magnetic fields between 200 and 400 Oe in the figure. The 8° angle between the microwave and static fields that was needed to obtain the Fig. 2 data yielded a combined parallel and transverse pumping response. The need for a reduced angle between the microwave field and the static field is related to FMR cavity coupling considerations which will be considered in Sec. III.

Figure 3 shows typical measurements of the microwave loss as a function of the microwave field amplitude. Graph (a) is for parallel pumping in the subsidiary loss regime; (b) is for resonance saturation at the FMR peak position; (c) is for resonance saturation for a static field somewhat above the FMR field point. The in-plane static field, H_{ext}, for each set of measurements is indicated in the graphs. The pump frequency was 8.93 GHz, the same as for Fig. 2. These data are for a 0.12 mm thick disk of the same Zn–Y material used for Fig. 2. Details of the measurement techniques will be given in Sec. III.

The three graphs in Fig. 3 demonstrate the threshold nature of the high power response. Figure 3(a) shows that in the subsidiary loss regime, the loss increases abruptly as the microwave field moves above threshold. Graphs (b) and (c) show that in the FMR regime, the loss can either increase or

Downloaded 02 Apr 2001 to 129.82.192.18. Redistribution subject to AIP copyright, see http://ojps.aip.org/japo/japcr.jsp

decrease abruptly as the microwave field moves above threshold, depending on the setting of H_{ext}. Precisely at resonance, one finds a decrease. Off resonance by some field shift on the order of the linewidth, one finds an increase.

The focus of the measurements and the analysis for this work is on the actual threshold or h_{crit} points indicated in Fig. 3. As indicated above, plots of h_{crit} versus static field are termed butterfly curves. Butterfly curves have been studied extensively for parallel pumping and subsidiary absorption in the subsidiary loss field regime, but most of this work has been for polycrystalline ferrites or cubic materials with low anisotropy. For resonance saturation, the focus has also been on low anisotropy materials and previous studies have focused only on the threshold response precisely at the FMR peak.

B. Instability theory

Detailed treatments of the spin wave instability theory are given by Suhl,[11] Schlömann,[15] Schlömann *et al.*,[16] Patton,[17,18] and Chen and Patton.[19] The purpose of this section is to establish working equations for explicit evaluations of h_{crit} as a function of H_{ext} for comparison with butterfly curve data. Equation details are given in the appendices. Section II C provides working equations for the uniform mode response and the spin wave dispersion relations for easy plane hexagonal ferrites which are needed for the analysis. Section II D discusses the procedure for critical mode and h_{crit} determinations. These details will be important for the discussion of the data and the h_{crit} analysis in Sec. IV.

As discussed by Schlömann,[15] a useful starting point for the spin wave instability theory is a general expression for the dynamic magnetization for a general mode at frequency ω_k and wave vector $\mathbf{k}$. Following Ref. 15, one may write this response in terms of a complex scalar magnetization response $m_k(t)$ in the form

$$m_k(t) = m_k \exp[i\omega_k t + (G_k - \eta_k)t]. \tag{1}$$

In Eq. (1), G_k represents the coupling rate for energy into the particular spin wave and η_k denotes the relaxation rate of that spin wave. The coupling coefficient G_k is a complicated function of the static and microwave magnetic fields, the pump frequency, the magnetization and anisotropy of the material, the shape of the sample, and the wave vector distribution of the available spin waves. The relaxation rate η_k is related to the spin wave linewidth ΔH_k introduced above.

The threshold for the instability occurs at the point in input power at which the condition $G_k = \eta_k$ is satisfied. Note that, as the power increases beyond this threshold point, the exponential term in Eq. (1) changes from negative to positive and yields an exponential growth as part of the $m_k(t)$ response. Higher order terms in the coupled uniform mode and spin wave dynamic equations limit this growth above threshold. The discussion here is concerned with the threshold point only and the h_{crit} which comes out of the $G_k = \eta_k$ analysis.

The end result is an explicit equation for the instability threshold h_{crit} as a function of the spin wave linewidth, the applied field, and other relevant microwave and materials parameters. A full review of spin wave instability theory is beyond the scope of this article. Chen and Patton[19] review threshold processes for the subsidiary loss region in isotropic ferrites. Schlömann *et al.*[16] discuss threshold processes for both the subsidiary loss and FMR regions for easy plane hexagonal ferrites such as Zn–Y. The theory in Ref. 16, however, does not consider FMR saturation processes, which occur off the peak of the resonance. The analysis outlined below extends the theory to include the field regime around the FMR point. An extended theory that covers general magnetization directions and anisotropy will be published separately.

As noted in the last section, there are important differences between PP, SA, and RS instability processes. The coupling coefficient G_k for the first order parallel pumping and subsidiary absorption processes scales with the microwave field amplitude h. For the second order resonance saturation process, G_k scales with the square of the microwave field. The strongest coupling for the PP and SA first order processes is for $\omega_k = \omega_p/2$. The strongest coupling for RS second order processes is for $\omega_k = \omega_p$. The formulation given below will reflect these differences.

As considered here, the field range for subsidiary absorption is well below the FMR field. This means that one is operating on the low field tail of the FMR response. From the equations in the Appendices, it will be clear that the actual FMR loss or linewidth does not enter into the response equations or into the expressions for G_k for first order processes, which occur well below the FMR field. For resonance saturation the linewidth will enter explicitly into the analysis.

For the analysis of first order thresholds, it is convenient to write G_k in the form

$$G_k^{(1)} = -\frac{|\gamma|}{2}\frac{\omega_m h}{\omega_p} W_k^{(1)} e^{2i\phi_A}. \tag{2}$$

The superscript (1) in $G_k^{(1)}$ now identifies the coupling parameter for first order processes only. The $|\gamma|$ in Eq. (2) is the absolute value of the electron gyromagnetic ratio. The ω_m parameter expresses the saturation induction in frequency units according to $\omega_m = |\gamma| 4\pi M_s$, where $4\pi M_s$ is the saturation induction of the ferrite. The $W_k^{(1)}$ factor is a reduced dimensionless coupling coefficient, which depends on the spin wave propagation direction and wave number, the FMR response, the microwave field polarization, and the anisotropy. The angle ϕ_A is related to the azimuthal spin wave propagation angle ϕ_k, but with modifications due to the easy plane anisotropy. Explicit equations for $W_k^{(1)}$ and ϕ_A are given in Appendix A.

One benefit of the form of Eq. (2) is that the linear dependence of the coupling on the microwave field amplitude h is made explicit. It is also convenient to express the spin wave relaxation rate η_k in terms of an equivalent spin wave linewidth ΔH_k according to $\eta_k = |\gamma| \Delta H_k/2$. In terms of these new parameters, Eq. (2) yields a formal expression for the first order spin wave instability threshold h_{crit} which may be written as

Downloaded 02 Apr 2001 to 129.82.192.18. Redistribution subject to AIP copyright, see http://ojps.aip.org/japo/japcr.jsp

$$h_{\rm crit}^{(1)}=\frac{\omega_p}{\omega_m}\min\left(\frac{\Delta H_k}{|W_k^{(1)}|}\right)_{\omega_k=\omega_p/2}. \tag{3}$$

The minimization is carried out over the available spin wave states at $\omega_k=\omega_p/2$. The range of such states is defined through the spin wave dispersion relation $\omega_k(\mathbf{k})$. The specific mode which yields the minimum threshold is termed the critical mode.

For the analysis of second order thresholds, it is convenient to write G_k in the form

$$G_k^{(2)}=\frac{\omega_m}{2}\left(\frac{h_t}{\Delta H_{\rm FMR}}\right)^2 W_k^{(2)}e^{2i\phi_A}. \tag{4}$$

Note the subscript ''*t*'' for the microwave field amplitude in Eq. (4). Only the transverse component of the microwave field is effective here. The parameter $\Delta H_{\rm FMR}$ denotes the usual low power ferromagnetic resonance linewidth at half power obtained from a field swept FMR measurement at the pump frequency ω_p. The $W_k^{(2)}$ factor is the resonance saturation counterpart to $W_k^{(1)}$. As with Eq. (2), Eq. (4) separates out the important functional dependencies on frequency, microwave field amplitude, etc., which control the $h_{\rm crit}$ threshold for resonance saturation. Precisely at the FMR peak position in field, the uniform mode response scales with $1/\Delta H_{\rm FMR}$ and this dependence is made explicit from the form of Eq. (4). Based on Eq. (4), the second order counterpart to Eq. (3) may be written as

$$h_{\rm crit}^{(2)}=\min\left(\Delta H_{\rm FMR}\sqrt{\frac{\Delta H_k}{4\pi M_s|W_k^{(2)}|}}\right)_{\omega_k=\omega_p}. \tag{5}$$

The combination of factors in Eq. (4), therefore, leads to a second order $h_{\rm crit}$ threshold which scales linearly with the FMR linewidth and with the square root of the spin wave linewidth. The minimization is now done over available states at the pump frequency. The range of these states is defined through the spin wave dispersion. Appendix B gives working equations for $W_k^{(2)}$.

The introduction of the dimensionless coupling parameters $W_k^{(1)}$ and $W_k^{(2)}$ serves several useful functions. First, and as noted above, these parameters make it possible to separate out the important functional dependencies of $h_{\rm crit}$ on frequency, magnetization, spin wave linewidth, and FMR linewidth. Second, in certain simple limits, the W_k parameters reduce to unity and one can recover simple threshold expressions for comparison with results for isotropic materials and simple geometries. In the case of parallel pumping in an isotropic sample for static fields below the butterfly curve minimum, for example, the $W_k^{(1)}$ parameter in Eq. (3) is equal to one. The parallel pump threshold then reduces to the well-known result from Schlömann, $h_{\rm crit}=(\omega_p/\omega_m)\Delta H_k$. In the case of ferromagnetic resonance in an isotropic sphere, the condition $W_k^{(2)}=1$ is satisfied. Equation (5) then yields Suhl's original resonance saturation threshold condition, which may be written as $h_{\rm crit}=\Delta H_k(\Delta H_k/4\pi M_s)^{1/2}$.

As the equations in the next section and in the appendices show, anisotropy results in significant complications in the analysis. A formulation in terms of $W_k^{(1)}$ and $W_k^{(2)}$ provides a simple way to set up the problem and provide convenient checks in simple limits.

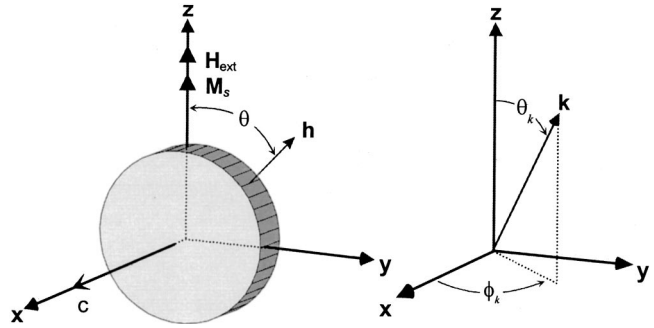

FIG. 4. Geometry for the easy plane disk sample with the hard *c* axis along the *x* direction, the static field $\mathbf{H}_{\rm ext}$ and the magnetization $\mathbf{M}_s$ is the *z* direction, the microwave field $\mathbf{h}$ in the *y*-*z* plane at an angle θ to the *z* axis, and the spin wave wave vector $\mathbf{k}$ with polar and azimuthal spin wave propagation angles θ_k and ϕ_k, as indicated.

C. Uniform mode response and spin wave dispersion

In general, the threshold evaluation involves the: (i) calculation of the uniform mode FMR response, (ii) determination of the spin wave dispersion, and (iii) minimization of the appropriate $h_{\rm crit}$ expression over the available spin wave states at the applicable value of ω_k. For an isotropic ferrite, the uniform mode response and spin wave dispersion relations are relatively simple, the scan over the available spin wave states is straightforward, and the critical mode is easily obtained.[19]

For hexagonal ferrites, both the uniform mode response and the spin wave dispersion equations are more complicated. This section reviews the relevant FMR response equations, provides working equations for the spin wave dispersion, and outlines the $h_{\rm crit}$ calculation procedure.

Figure 4 shows the geometry for a Zn–Y disk sample with the easy plane in the disk plane, a static and microwave field configuration which matches the experiment, and a suitable spin wave wave vector convention for dispersion definitions. The left diagram shows the disk orientation in the easy *y*-*z* plane with the static magnetic field $\mathbf{H}_{\rm ext}$ and the static magnetization $\mathbf{M}_s$ along the *z* axis. The linearly polarized microwave field $\mathbf{h}$ is also in the *y*-*z* plane and is at an angle θ to the *z* axis. The hard hexagonal *c* axis is in the *x* direction. The diagram on the right shows the spin wave wave vector $\mathbf{k}$ with polar and azimuthal propagation angles θ_k and ϕ_k, respectively.

For the geometry of Fig. 4, the uniform mode FMR frequency[16] may be obtained in the form

$$\omega_{\rm FMR}=|\gamma|\sqrt{H_aH_b}, \tag{6}$$

where the two stiffness fields H_a and H_b are given by

$$H_a=H_{\rm int}+4\pi M_sN_x+H_A, \tag{7}$$

and

$$H_b=H_{\rm int}+4\pi M_sN_y. \tag{8}$$

Downloaded 02 Apr 2001 to 129.82.192.18. Redistribution subject to AIP copyright, see http://ojps.aip.org/japo/japcr.jsp

In the above equations, $H_{\text{int}}=H_{\text{ext}}-4\pi M_s N_z$ is the z-directed static internal field and the $N_{x,y,z}$ parameters denote the disk demagnetizing factors based on the ellipsoidal sample shape approximation.[20] The H_A parameter denotes an effective field that characterizes the planar anisotropy and is taken to be positive. Note that H_a is the total stiffness field for a tipping of the magnetization out of the disk and easy anisotropy plane. This effective stiffness field, therefore, includes the indicated H_A component in addition to the applied static field and demagnetizing field terms in the Kittel condition.[21] The H_b field for tipping in the film plane contains no such additional anisotropy term.

The spin wave dispersion equation may be written in a form similar to Eq. (6):

$$\omega_k=|\gamma|\sqrt{H_a H_\beta+H_\gamma^2}. \tag{9}$$

The H_α and H_β terms denote spin wave stiffness fields and H_γ is an additional term which arises from the low symmetry:

$$H_\alpha=H_{\text{int}}+Dk^2+4\pi M_s\sin^2\theta_k+H_A, \tag{10}$$

$$H_\beta=H_{\text{int}}+Dk^2, \tag{11}$$

$$H_\gamma=\sqrt{H_A 4\pi M_s}\sin\theta_k\sin\phi_k. \tag{12}$$

The D parameter is an exchange coefficient and k denotes the spin wave wave number. The exchange is taken as isotropic. In the limit of zero anisotropy, Eqs. (9)–(12) reduce to the well known isotropic bulk spin wave dispersion relation first developed by Kittel.[22]

Numerical values for the various sample parameters needed for h_{crit} and critical mode evaluations are given in Sec. III. However, several comments are appropriate here. First, for the configuration of Fig. 4, N_x is close to unity and the $N_{y,z}$ demagnetizing factors are close to zero. The numerical evaluations given below are based on the D value for yttrium iron garnet, 5.4×10^{-9} Oe cm^2/rad^2. There is some evidence that the exchange field terms for hexagonal ferrite are anisotropic and vary with propagation direction.[23] These effects are not considered here.

Figure 5 shows a representative set of spin wave dispersion curves for a thin disk when the static field is close to the FMR field for resonance. These specific results are based on parameters for the 0.1 mm thick disk, referred to as sample S2 in the next section, and a static field of 850 Oe. The graph shows the spin wave frequency as a function of the wave number k for the three principal dispersion branches, as indicated. The solid circle at about 9 GHz on the vertical axis, and the dashed line which crosses the two lower curves, indicate the FMR frequency.

The spin wave band consists of the region between the lower and upper curves. While the upper and middle curves are for the same polar propagation angle $\theta_k=90°$, the azimuthal propagation angle ϕ_k for these curves is at 90° and 0°, respectively. This provides an explicit demonstration of the complicated nature of the constraint on available modes for the $h_{\text{crit}}^{(1)}$ and $h_{\text{crit}}^{(2)}$ evaluations of Sec. II B. See Hurben *et al.*[24] for a more detailed discussion of such spin wave manifolds.

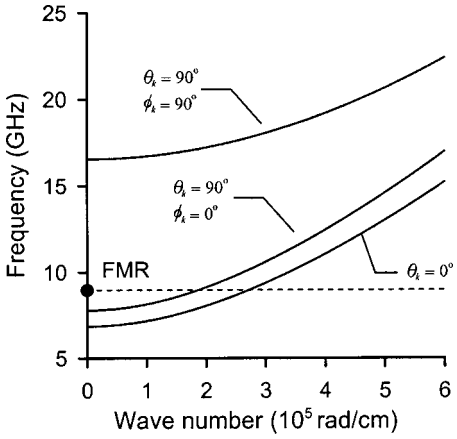

FIG. 5. Computed spin wave dispersion curves of frequency vs wave number for different spin wave propagation directions, as indicated. The curves are for parameters which match sample S2 and a static field of 850 Oe. The solid circle and the FMR label indicate the corresponding ferromagnetic resonance frequency.

Because the spin wave band shifts with field, the ranges of θ_k, and ϕ_k for spin wave modes at either ω_p or $\omega_p/2$ will also shift. Within these allowed angle ranges, k may be obtained from the dispersion equations. One can see from Fig. 5 that there are three regions. At very low fields, and if the frequency of interest is above the $k=0$ intersection point for the upper branch, all values of θ_k and ϕ_k between 0° and 90° are allowed. For a range of intermediate fields, with the frequency between the $k=0$ intersection points for the two highest branches, all θ_k values are allowed if ϕ_k is below the critical value indicated above. For ϕ_k above this value, the maximum θ_k will be a function of ϕ_k. For a range of high fields for which the frequency point is between the $k=0$ intersection point for the two lowest branches, the maximum θ_k will be a function of ϕ_k over the entire range, $0°\leqslant\phi_k\leqslant90°$.

The above conditions, in combination with the dispersion equations, the FMR condition, and the specification of a first or second order instability process, provide all of the criteria needed to perform the minimizations implicit in Eqs. (3) and (5). From this procedure, one obtains h_{crit}, as well as the critical modes responsible for this minimum threshold as a function of the static field for the configurations of interest. The details of the calculations will not be given here. One simply establishes the range of values of θ_k, and ϕ_k for the available modes constructs an appropriate grid of these angles and searches this grid for the minimum threshold.

III. EXPERIMENT

A. Materials

The Mn substituted single crystal Zn Y-type (Zn–Y) hexagonal ferrite materials were grown at Purdue University by standard techniques and with a $2BaO-B_2O_3$ flux.[5,25,26] A commercial composition analysis of the material gave a Mn concentration of 2.6% by weight. This corresponds to a nominal formula unit of $Ba_2Zn_{2-x}Fe_{12-y}Mn_{x+y}O_{22}$, subject to the condition $x+y=0.7$. The manganese substitution compensates for any residual Fe^{2+} that may be present. This,

Downloaded 02 Apr 2001 to 129.82.192.18. Redistribution subject to AIP copyright, see http://ojps.aip.org/japo/japcr.jsp

TABLE I. Sample parameters for the three Mn substituted Zn–Y disk shaped samples. The symbolic headers give the saturation magnetization $4\pi M_s$, the anisotropy field H_A, the out of plane demagnetizing factor N_z, the electron gyromagnetic ratio absolute value $|\gamma|$ divided by 2π, the static magnetic fields required to saturate the sample in the disk plane, $H_{\text{sat-in}}$, and out of the disk plane, $H_{\text{sat-out}}$, the first order butterfly curve cut off field H_{cut}, the ferromagnetic resonance (FMR) field H_{FMR}, and the FMR linewidth ΔH_{FMR}.

Sample	Thickness (mm)	$4\pi M_s$ (kG)	H_A (kOe)	N_z	$\lvert\gamma\rvert/2\pi$ (GHz/kOe)	$H_{\text{sat-in}}$ (Oe)	$H_{\text{sat-out}}$ (kOe)	H_{cut} (Oe)	H_{FMR} (Oe)	ΔH_{FMR} (Oe)
S1	0.090	2.957	9.500	0.054	2.84	—	—	413	775	16
S2	0.113	2.992	9.668	0.077	2.715	230	12.20	502	845	10
S3	0.205	2.855	9.335	0.130	2.72	380	11.50	650	900	14

in turn, serves to maintain a high resistivity material and eliminate eddy current complications in the microwave response which are found in materials without Mn substitution.[8] Such unsubstituted materials have a conductivity at 10 GHz of about 0.04 $\Omega^{-1}\,\text{cm}^{-1}$.[8] Savage *et al.*[26] have shown that Mn doping can increase the resistivity of the ferrite by approximately three orders of magnitude.

Disks shaped samples were fabricated from as grown *c*-plane platelets of the crystals described above. The particular samples used for the data reported below were obtained from three platelets with nominal thicknesses of 90, 100, and 200 μm. The edges of the platelets were ground with silicon carbide 600 grit paper and polished with 1 μm alumina powder. The final disks were near circular and nominally 1 mm in diameter. The virgin flat surfaces of the platelets were left untouched. For convenience, these disks, in order of increasing thickness, will be denoted as samples S1, S2, and S3. The thinnest sample, S1, most closely resembled a cylindrical disk. The edges of the other two samples were somewhat beveled.

Various sample parameters are needed for the theoretical threshold evaluations in Sec. IV. The important materials parameters are $4\pi M_s$, H_A, and $|\gamma|$. The demagnetizing factors $N_{x,y,z}$ and the FMR linewidth ΔH_{FMR} also enter into the formulas summarized above and in the Appendices. The remaining parameter, the spin wave linewidth ΔH_k, will be used as a fitting parameter to match theory to experiment.

Self-consistent values of $4\pi M_s$, H_A, $|\gamma|$, and the out of plane demagnetizing factor N_x were obtained from measurements of saturation fields, the high field cutoff point for the parallel pumping butterfly curve, and the low power FMR peak position. The theoretical in-plane and out-of-plane saturation fields may be written as

$$H_{\text{sat-in}} = 4\pi M_s N_y . \tag{13}$$

and

$$H_{\text{sat-out}} = H_A + 4\pi M_s N_x , \tag{14}$$

respectively. These saturation fields were determined from magnetization versus field data obtained by vibrating sample magnetometery measurements. The expression for the first order butterfly curve cutoff field H_{cut} for SA and PP processes is the field obtained from Eq. (9) with ω_k set to $\omega_p/2$ and k and θ_k both set to zero. The FMR field, H_{FMR}, is given by the H_{ext} expression obtained from Eq. (6) with ω_{FMR} set equal to ω_p. One has, therefore, four equations and four unknowns, the $4\pi M_s$, H_A, $|\gamma|$, and N_x parameters listed above.

The FMR half power linewidth was obtained from low power loss profiles similar to the data in Fig. 2. All of the microwave measurements, high power as well as low power, were made at a pump frequency of 8.93 GHz with the system described below. The measured linwidths for samples S1, S2, and S3 were 16, 10, and 14 Oe, respectively. These values are reasonably small for single crystal Zn–Y. Typical Zn–Y linewidths from the literature are in the 8–30 Oe range at 10 GHz.[25] Savage *et al.*[26] report one sample with a 3.8 Oe linewidth at 9 GHz, but this appears to be an exception to the rule.

Sample parameters are listed in Table I. Sample S1 was damaged before the analysis was completed. For this sample, the demagnetizing factors were estimated from the Osborn analysis,[20] H_A was set to the average value obtained for S2 and S3, and $4\pi M_s$ and $|\gamma|/2\pi$ were obtained from the FMR field and the butterfly curve cutoff field. The parameters listed in Table I are consistent with literature values. Note that H_{cut} and H_{FMR} become larger as one moves from sample S1 to sample S3. This is due to the increase in N_z with disk thickness.

B. Microwave measurements

The microwave measurements were made with a reflection cavity microwave spectrometer similar to the system described by Zhang *et al.*[27] Figure 6 shows a schematic of the system. The spectrometer proper consists of a pulsed

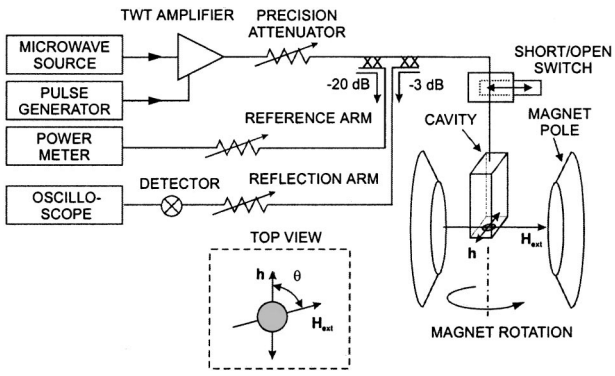

FIG. 6. Schematic diagram of the high power reflection cavity microwave spectrometer. The inset shows a schematic top view of the sample and the field geometry. The sample is centered on the bottom end wall of the cavity with the static applied magnetic field $\mathbf{H}_{\text{ext}}$ and the microwave magnetic field $\mathbf{h}$ as indicated, with both fields in the plane of the disk and at a relative angle θ. The electromagnet was rotated about a vertical axis, as indicated, to set the angle θ.

Downloaded 02 Apr 2001 to 129.82.192.18. Redistribution subject to AIP copyright, see http://ojps.aip.org/japo/japcr.jsp

microwave source, an input microwave line and cavity section, a reference arm, and a reflection arm. The cavity and sample are in the gap of a rotatable electromagnet. The dashed box inset shows the sample and the field geometry.

The pulsed microwave source consists of a Hewlett Packard HP83640A frequency synthesizer, an Applied Systems Engineering Model 174XKU traveling wave tube (TWT) amplifier, and a Wavetek Model 81 pulse generator. The synthesizer provides a 0 dBm cw signal to the TWT amplifier. The pulse generator provides a gate signal to the TWT amplifier for the generation of microwave pulses up to 2 kW in peak power, 100 μs in length, and with a maximum duty cycle limit of 4%. The microwave pulse rise time was about 100 ns. Pulse widths of 10 and 50 μs were used for the near resonance and subsidiary loss measurements, respectively. The shorter pulse widths were needed for the resonance measurements in order to avoid heating effects. The longer pulses were needed for the subsidiary loss measurements in order to obtain accurate threshold determinations. Additional pulse width and duty cycle considerations are examined below. The nominal operating frequency was 8.93 GHz. The frequency was adjusted to match the field and sample dependent cavity frequency, as needed.

The input microwave section consists of a high power isolator, a precision attenuator, a waveguide short/open switch, and a reflection cavity. The rectangular TE_{101} cavity was under coupled. The empty cavity had a nominal reflection coefficient of -17 dB at cavity resonance and a nominal loaded quality factor Q_L of 2100. The cavity Q factors were determined by the technique given in Ref. 28.

The reference and reflection arms in Fig. 6 serve to monitor the powers incident on and reflected from the cavity, respectively. The reference arm is coupled to the main line with a 20 dB directional coupler and is terminated with an HP 436A microwave power meter. After calibration for line loss, the measured average power divided by the duty cycle gives the peak input power at the cavity, P_{in}. The reflection arm is coupled to the main line with a 3 dB directional coupler and is terminated with an HP 8474D microwave detector. The reflection arm attenuator is an HP X382A precision attenuator. It is used in conjunction with the short/open switch in the cavity line and a digital oscilloscope connected to the detector to measure the cavity reflection coefficient. The reference and reflection arm attenuators both serve to protect the sensitive detection components in the power meter head and the microwave detector, respectively.

The dashed line inset in Fig. 6 shows a top view of the disk sample. The vectors indicate the static external magnetic field $\mathbf{H}_{\text{ext}}$ and the microwave pump field $\mathbf{h}$ in the plane of the disk. The angle θ between $\mathbf{H}_{\text{ext}}$ and $\mathbf{h}$ is shown in the inset. This angle could be changed through rotation of the electromagnet.

The system in Fig. 6 was used for low and high power absorption curve measurements of the sort shown in Fig. 2 and loss versus microwave field measurements as shown in Fig. 3. For measurements over the range of fields near the FMR peak position, it was necessary to use a relatively small angle between $\mathbf{H}_{\text{ext}}$ and $\mathbf{h}$ in order to reduce the coupling between the FMR resonance response and the cavity. Typically, this angle was set such that the drop in the cavity Q due to the FMR resonance response was never more than 10% of the off resonance low power value. This is the reason for the $\theta = 8°$ setting for the data in Fig. 2 and in images (b) and (c) of Fig. 3. In these cases, only the component of the microwave field transverse to the static field drives the response. Cavity loading problems at ferromagnetic resonance are often solved through the use of a lower Q cavity. In the present case, such a solution would sacrifice the sensitivity that is needed for the near resonance measurements.

For measurements in the subsidiary loss regime, θ was set at 0° or 90° for the parallel pumping and subsidiary absorption measurements, respectively. For these measurements, one is sufficiently far from ferromagnetic resonance to avoid cavity loading problems.

An additional advantage of the angle rotation capability is in the ability to change between pumping configurations without any disassembly and reassembly of waveguide and cavity components. Such disassembly and reassembly often leads to changes in cavity parameters and the need for recalibration. The arrangement in Fig. 6 avoids these problems. Calibration considerations are discussed below.

In addition to the cavity loading issues considered above, accurate high power measurements require careful attention to two other factors, the pulse width and the duty cycle. As discussed in Sec. II, spin wave instability involves the growth of parametric spin waves when the power exceeds a given threshold. There is always some characteristic time for such processes to take place and for the microwave response to reflect this change. If the microwave pulse is too short, one will obtain threshold values that are too large.[12] A pulse width which is too long will lead to sample heating and thresholds that are too low.[29] Sample heating is of special concern for high power measurements near resonance because of the large losses which are present even below threshold. The resonance saturation data reported here were obtained for a duty cycle of 0.1% and input pulse widths of 10 μs. Larger duty cycles or longer pulses resulted in observable heating effects. For the subsidiary loss regime, where the low power losses are much lower and these parameters are not as critical, the pulse width was increased to 50 μs and the duty cycle was maintained at 0.1%.

C. Microwave field configuration and calibration

The one remaining experimental consideration is the calibration procedure to obtain the microwave field amplitude at the sample as a function of the power incident on the cavity, P_{in}. One may obtain a direct connection between P_{in} and the microwave field amplitude at any point inside the cavity from electromagnetic theory. For the applicable sample position at the center of the end wall of a reflection cavity operated at the cavity resonance frequency f_{res}, the microwave field amplitude h may be written as[30]

$$h(\text{Oe}) = \sqrt{\frac{40 Q_L (1-\rho)}{g f_{\text{res}}(\text{GHz}) V(\text{mm}^3)}} [P_{\text{in}}(\text{W})]^{1/2}. \tag{15}$$

In Eq. (15), Q_L is the loaded Q of the cavity, ρ is the voltage reflection coefficient of the cavity at resonance, and V is the

Downloaded 02 Apr 2001 to 129.82.192.18. Redistribution subject to AIP copyright, see http://ojps.aip.org/japo/japcr.jsp

cavity volume. The g parameter in Eq. (15) relates the stored energy in the cavity to the microwave field amplitude.[31] For the TE101 cavity used here, g may be written as

$$g=\tfrac{1}{8}[1+(l/a)^2], \tag{16}$$

where l and a are the cavity length and width, respectively.[30]

Note the dimension specific parameters in Eq. (15). The voltage reflection coefficient ρ in Eq. (15) is related to the usual reflection measurement in dB, Γ, according to $\rho=10^{\Gamma/20}$. The convention has been adopted to use ''f'' parameters to denote frequencies in Hz or related units. Frequencies denoted by the various ''ω'' parameters (see Sec. II), are typically taken to be angular frequencies expressed in rad/s.

For the TE101 reflection cavity used here, the nominal values of Q_L and Γ were 2100 and -17 dB, respectively. The nominal cavity frequency was 8.93 GHz and the calibration ratio h^2/P_{in} from Eq. (15) was 5.1 Oe^2/W. Note that the corresponding formula in Ref. 31 is for the microwave field at the center of the cavity side wall, while the diagram in the article indicates, incorrectly, the center of the end wall as the microwave field position.

For a given measurement or set of measurements and a given input peak microwave power, Eq. (15) was used to calibrate the microwave field at the sample position. This result, however, is based on the empty cavity analysis. Such a calibration is valid only to the extent that the sample does not affect the cavity mode upon which Eqs. (15) and (16) are based. Two aspects of the measurement procedure address this issue. First, the empty cavity Q_L and ρ values were always close to the corresponding values for the cavity at high field and low power with a sample in place. The differences varied from sample to sample, but were on the order of 2%. The small effect of the sample on the response gives a qualitative indication that the cavity mode structure is almost the same with and without the sample. Second, and as pointed out above, the loaded cavity Q was never allowed to drop more than 10% relative to the reference Q_L value for a given measurement. As an additional check on calibration, data were obtained for several standard commercial ferrite samples for which h_{crit} values are well established.

IV. RESULTS

A. Resonance saturation

Typical experimental results on resonance saturation are shown in Fig. 7. Graph (a) shows resonance saturation butterfly curves of the spin wave instability threshold microwave field amplitude h_{crit} as a function of H_{ext} for a nominal pump frequency of 8.93 GHz. The high power data for samples S1 and S2 are shown as the solid and open circles, respectively. Graph (b) shows low-power FMR absorption curves of normalized microwave loss versus the static external magnetic field. For (b), the angle θ between the in-plane static and microwave fields was set at 8°. For the data in (a), this angle was also set at 8° for the h_{crit} measurements at the FMR point. For h_{crit} measurements away from the FMR field, this angle was increased as needed to achieve higher sensitivity to about 60° for the extreme end point data in the figure. As discussed above, it was necessary to use small θ values for measurements at or near the FMR point in order to reduce cavity loading. The S1 data in (b) are the same as in Fig. 2.

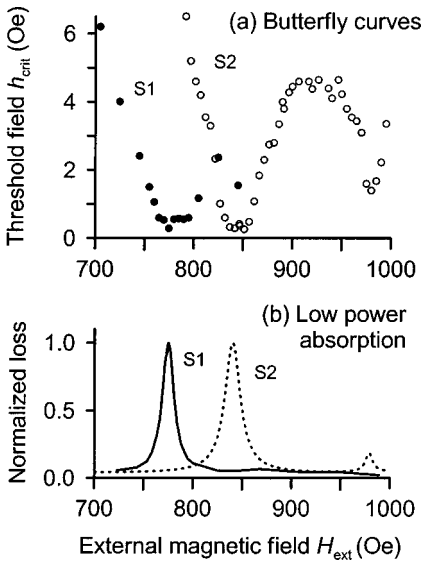

FIG. 7. (a) Resonance saturation butterfly curves of the spin wave instability threshold microwave field amplitude h_{crit} vs. H_{ext} for Zn–Y c-plane disk samples S1 and S2, as indicated. The nominal operating point frequency was 8.93 GHz and (b) low power ferromagnetic resonance absorption curves of loss vs. static external magnetic field H_{ext}.

The low power FMR curves in (b) are typical for Zn–Y c-plane disks. The difference in the FMR peak positions for the two disks is mainly due to the different thicknesses and the corresponding difference in the demagnetizing factors. In addition to the prominent primary FMR absorption peaks, the absorption curves also show secondary peaks at higher fields. These peaks are associated with magnetostatic mode (MSM) resonances. The MSM peak is clearly visible in the S2 data and is less pronounced for the S1 data.

The butterfly curves in (a) demonstrate the correlation between the low power FMR response and the h_{crit} threshold field behavior. The minimum thresholds for both samples occur at $H_{\text{ext}}=H_{\text{FMR}}$. On either side of the main FMR peak position, as long as one is within about one linewidth of the peak, there is little change in h_{crit}. However, as one moves further away from the peak, the thresholds increase rapidly and dramatically.

It is also important to note the effect of the MSM resonances on the h_{crit} response. The MSM peak in (b) for sample S2 is centered at about 980 Oe. At this same point in field, there is a second minimum in the h_{crit} data. The apparent drop in h_{crit} for fields above about 825 Oe for sample S1 may also be due to a MSM effect. This drop occurs at about the same external magnetic field for which the low power absorption curve turns upward. The MSM peak for sample S1 is much weaker and the high power data go only to 850 Oe.

The data in Fig. 7(a) represent the first actual measured butterfly curves for resonance saturation to be reported in the literature. All previously reported resonance saturation h_{crit} measurements have been limited to the thresholds at H_{ext}

Downloaded 02 Apr 2001 to 129.82.192.18. Redistribution subject to AIP copyright, see http://ojps.aip.org/japo/japcr.jsp

$=H_{\mathrm{FMR}}$ only. In this article, work for any ferrite material has examined the field dependence of the h_{crit} threshold and provided actual butterfly curve profiles for this dependence. As discussed below, such data give new information on the threshold response and on the spin wave loss processes which are not apparent from measurements only at the FMR point.

In qualitative terms, the results are as one would expect. The reduced amplitude for the uniform mode response away from resonance results in a decrease in the $W_k^{(2)}$ factor in Eq. (5), and a corresponding increase in the h_{crit} threshold. In quantitative terms, however, there are two new results from Fig. 7(a). First, there is a rather rounded h_{crit} response for fields near resonance. Second, there is a sharper ''V'' shaped response with a small but distinct asymmetry in the butterfly curve for fields outside the rounded region.

Both effects are unexpected. First consider the rounded h_{crit} response. One would expect the increase in h_{crit} as one moves away from the FMR peak position in field to mirror the drop in the FMR response. The data in Fig. 7 show that this is not the case. The data show that the threshold seems to respond rather weakly to the drop in the FMR amplitude until one is away from the FMR field by a linewidth. Then, and only then, does the threshold show an increase.

Now consider the asymmetry. The low power FMR absorption line is essentially symmetric, whereas the threshold field data show that this symmetry is not transferred to the resonance saturation butterfly curve profile. Rather, the data show that the rate of increase for h_{crit} as one moves out of the rounded response region is greater for fields below resonance than for fields above the FMR point.

Figure 8 shows the butterfly curve data from Fig. 7 for sample S2 along with computed h_{crit} versus H_{ext} curves and the corresponding critical mode k values as a function of field, based on the theory. In Fig. 8(a), the solid circles show the same S2 data as previously and the dashed and solid lines show the calculations. The solid curve is for a fixed, **k** independent ΔH_k value of 7.0 Oe. The h_{crit} minimization was done over all allowed values of θ_k and ϕ_k, and the minimum threshold always occurred for $\theta_k=0$. The dashed curve is for a **k** dependent spin wave linewidth of the form $\Delta H_k=Bk$, with B equal to 7.5×10^{-5} Oe cm/rad and θ_k held at zero. As noted below, the $\theta_k=0$ condition is the same as expected from the Suhl theory for isotropic materials. These ΔH_k parameters were chosen to match the shapes of the h_{crit} vs. H_{ext} responses over the rounded region near FMR and for the ''V'' characteristic away from FMR, respectively. Figure 8(b) shows the calculated critical mode wave number k vs. field profile, which corresponds to both of the theoretical butterfly curves in Fig. 8(a). Note that the two fits do not give the same minimum threshold values. The critical mode at the butterfly curve minimum has a k value of about 2.7×10^{-5} rad/cm. Therefore, the calculated spin wave linewidth is ~20 Oe at the butterfly curve minimum. This factor of three differences in ΔH_k between the two fits translates into a factor of two differences in the minimum theoretical thresholds, based on the square root ΔH_k factor in Eq. (5).

The computed butterfly curves in Fig. 8(a) provide an indication of some of the effects that control the h_{crit} response. It is to be noted that with B equal to 2.5×10^{-5} Oe cm/rad and θ_k held at zero one obtains almost the same result as shown by the solid curve for the $\Delta H_k=A$ form of the spin wave linewidth. These fits replicate the rounded butterfly curve near FMR response quite well. At the same time, the dashed curve for $\Delta H_k=Bk$ and the larger B-value models the data away from the central FMR region reasonably well. The asymmetry noted above is due to the decrease in the wave number of the excited spin waves with increasing field.

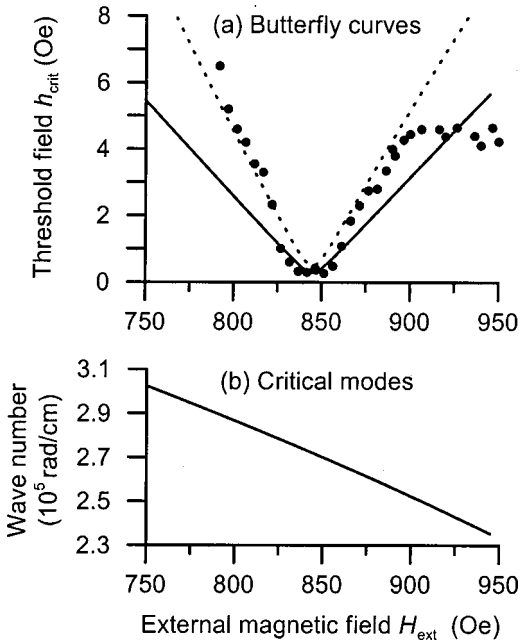

FIG. 8. (a) Resonance saturation butterfly curves of the threshold microwave field amplitude h_{crit} vs the static external magnetic field H_{ext} for Zn–Y c-plane disk sample S2. The solid circles show the same data as in Fig. 6. The solid line shows the computed results for a **k** independent spin wave linewidth of 7 Oe. The dashed line is for a linearly **k** dependent spin wave linewidth of the form $\Delta H_k=Bk$ with B equal to 2.5×10^{-5} Oe cm/rad. (b) Plot of critical mode wave number k vs. H_{ext} which corresponds to both of the computed curves in (a).

The different fits in Fig. 8 may be taken as an indication that there is a fundamental change in the form of $\Delta H_k(\mathbf{k})$ as one moves from the FMR peak region out to the tails of the FMR response. In the absence of a quantitative theory, no effort was made to examine a wider range of $\Delta H_k(\mathbf{k})$ functions. While it is not clear how or why there is a change in $\Delta H_k(\mathbf{k})$ for resonance saturation, it is to be noted that similar effects occur for oblique pumping in single crystal YIG.[32] In the case of second order Suhl processes in the vicinity of FMR, this transition may be related to some sort of saturation process. One might speculate that the large uniform mode amplitude close to FMR drives the spin waves to very high amplitudes, and that this leads to a washing out of the k dependence for ΔH_k. Further work, both experimental and theoretical, is needed to clarify these effects.

As noted above, the critical mode θ_k value of 0° for the constant ΔH_k fit is the same as expected from the original Suhl analysis for isotropic materials.[11] The fact that the calculated critical mode propagation angle is parallel to the static field means that the azimuthal angle dependence for the spin wave dispersion does not play an important role for

Downloaded 02 Apr 2001 to 129.82.192.18. Redistribution subject to AIP copyright, see http://ojps.aip.org/japo/japcr.jsp

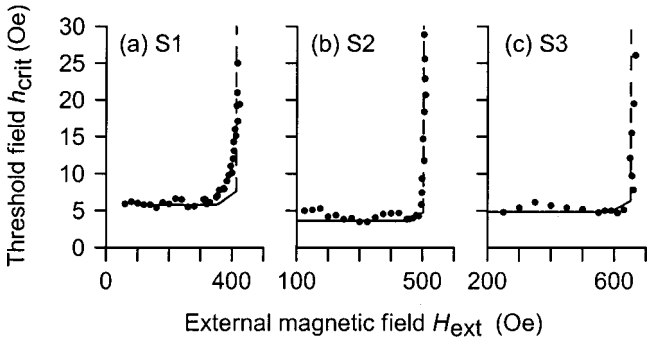

FIG. 9. Parallel pump butterfly curves of the spin wave instability threshold microwave field amplitude h_{crit} vs the static external magnetic field H_{ext} for Zn–Y *c*-plane disk samples S1, S2, and S3, as indicated. The data and theory are shown by the solid points and solid lines, respectively. The vertical dashed lines show the cutoff point for first order processes at $H_{ext}=H_{cut}$. The nominal operating point frequency for the measurements and the pump frequency for the calculations was 8.93 GHz.

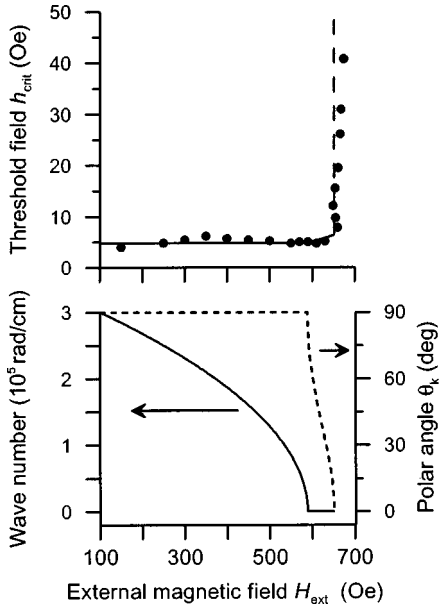

FIG. 10. Parallel pump butterfly curve and critical mode results for sample S3. The upper graph shows the threshold vs field data and the computed butterfly fit from Fig. 9(c). The data and theory are shown by the solid points and solid line, respectively. The vertical dashed line shows the cutoff point for first order processes at $H_{ext}=H_{cut}$. The lower graph shows the critical mode wave number k and polar angle θ_k vs. H_{ext}.

resonance saturation. The critical mode k value at the FMR field also appears to have no special significance. This gives further support to some sort of saturation effect for $\Delta H_k(\mathbf{k})$ at fields near the ferromagnetic resonance point. Here too, further work is needed. Brillouin light scattering measurements for resonance saturation in single crystal YIG films indicate that the critical mode θ_k value is 90° rather than at the 0° value from the Suhl theory.[33]

B. Parallel pumping

Figure 9 shows parallel pumping butterfly curve results for the three samples, as indicated. The solid circles and the solid lines show the data and the theoretical fits, respectively. The vertical dashed lines indicate the cutoff point for each of the theoretical curves at $H_{ext}=H_{cut}$. The three graphs all show the same general features. (1) The h_{crit} values for a relatively wide range of static fields are all around 4.5–7.5 Oe. (2) There is a cutoff static field at which h_{crit} appears to diverge rapidly. As discussed below, the fixed threshold at low field indicates a **k** independent spin wave linewidth for parallel pumping. The cutoff fields correspond to the H_{cut} values in Table I. The gradual shift in H_{cut} to higher fields as one moves from S1 to S2 to S3 is due to the increase in disk thickness and in the in-plane demagnetizing factor. Similar shaped parallel pump butterfly curves have been published in the literature.[34–36]

The computed butterfly curve fits in Fig. 9 were obtained with the parameters listed in Table I, as needed. A fixed value of the spin wave linewidth parameter was used in each case to obtain the best match with the fixed h_{crit} values at low static fields. These fitted ΔH_k values for samples S1, S2, and S3 were 24, 14, and 18 Oe, respectively. The relatively wide range of the low field h_{crit} and the corresponding ΔH_k values for similar samples matches the findings in the work cited above by Tauber and co-workers.[37]

Note the small but distinct corner in all of the computed butterfly curves close to the high field cutoff point. This effect is clearly evident from the solid curve in (a) and present but less apparent in (b) and (c). These corners are due to a combination of effects; (1) a critical mode ϕ_k value of 0° over the entire range of static fields for the parallel pumping response, and (2) the extreme warp in the $\theta_k=90°$ dispersion surface and the extremely narrow width for the spin wave band at $k=0$ and $\phi_k=0°$ which results from this warp (see Fig. 5). As discussed below, the $\theta_k=90°$ and $\phi_k=0°$ critical mode conditions, where allowed, are related to the preference of a high ellipticity for the modes with the lowest threshold.

This corner response also contains a second effect which is special for hexagonal ferrites. This effect consists of a finite value of h_{crit} for the high field corner point at $H_{ext}=H_{cut}$. For isotropic ferrites, the spin wave precession is strictly circular at this butterfly curve cutoff point. This leads to a h_{crit} which increases rapidly as H_{ext} approaches H_{cut} and diverges to infinity at $H_{ext}=H_{cut}$. For planar ferrites magnetized in the easy plane, the critical mode has elliptical polarization even in the $H_{ext}=H_{cut}$ limit, and this keeps the threshold field finite at cutoff. The theoretical curves in Fig. 9 show this finite threshold at cutoff by the truncated solid lines at $H_{ext}=H_{cut}$ and the vertical dashed lines which extend vertically from this point.

The S2 and S3 data in Fig. 9 show these effects to varying degrees. In both cases, the experimental butterfly curves exhibit a very rapid divergence at $H_{ext}=H_{cut}$. While there may be an experimental corner effect for these two samples, the resolution in h_{crit} is not sufficient to establish the effect unambiguously. The S2 data show a rapid increase in h_{crit} as one approaches $H_{ext}=H_{cut}$, but there is no evidence of either the corner effect or the finite threshold at the cutoff point.

Figure 10 shows the parallel pump butterfly curve data and fit from Fig. 9(c) on an expanded scale and an additional graph with details on the critical mode behavior as a function of H_{ext}. The left and right vertical axes in the bottom graph

Downloaded 02 Apr 2001 to 129.82.192.18. Redistribution subject to AIP copyright, see http://ojps.aip.org/japo/japcr.jsp

show the critical mode k and θ_k values, respectively. The critical mode azimuthal angle ϕ_k remain at 0° for the entire range of fields for the butterfly curve.

The critical mode behavior can be divided into two parts. For external fields below about 590 Oe, the critical mode polar propagation angle θ_k is constant at 90° and there is a smooth and continuous decrease in the critical mode k value from about 3×10^5 rad/cm to zero. As discussed above, spin wave ellipticity considerations give the strongest coupling for $\phi_k=0$ and $\theta_k=90°$ and these conditions determine the critical mode response. From $H_{ext}\approx590$ Oe to the high field butterfly curve cutoff point at $H_{ext}=H_{cut}=650$ Oe, $\theta_k=90°$ is no longer allowed and this forces the smooth drop in θ_k from 90° to 0 with ϕ_k and k both maintained at zero. This second region is the origin of the characteristic butterfly curve corner close to the high field cutoff point in the upper graph of Fig. 10 and, as already noted, in all three of the theoretical butterfly curves of Fig. 9.

These parallel pump results give a good indication of the intrinsic relaxation rate in single crystal Zn–Y materials as well as the critical mode response. The results also raise a number of questions. The main question is, ''Why are these spin wave linewidths so large?'' These samples were made from single crystal platelets with low conductivity. The parallel pump process is expected to yield a intrinsic spin wave linewidth value that is independent of inhomogeneous broadening effects, such as two magnon scattering processes, and other nonintrinsic processes.[38] Yet, the measured ΔH_k values range from 14 to 24 Oe. These values are a factor of ten or larger than expected for good single crystals of spinel ferrite[39,40] or garnet materials.[41] It is to be noted as well that these parallel pump spin wave linewidths are larger than those found for resonance saturation. These larger ΔH_k values occur even though the predicted critical modes are at one-half the pump frequency. Recall that the critical modes for resonance saturation are at the pump frequency.

Further work to identify the origin of these large parallel pump spin wave linewidths in Y-type hexagonal ferrite materials is clearly needed. Several past studies have focused on the FMR linewidth and the high field effective linewidth.[8,9] These investigations have demonstrated (1) that there are significant inhomogeneities present in these single crystals and (2) that they strongly affect the relaxation rate at high field as well as the linewidth at ferromagnetic resonance.[8,42]

The second question concerns the characteristic corner shapes for the theoretical butterfly curves in Figs. 9 and 10. Here the question is ''Why are these characteristic corners not consistently resolved in the experiment?'' From Fig. 9, one sees a variety of experimental results. For sample S1, the increase in h_{crit} as the static field approaches H_{cut} is gradual and the h_{crit} values fall well above the theoretical corner shaped response. For samples S2 and S3, the increases in h_{crit} at the band edge are much sharper, but there is still no clearly resolved corner effect from the data.

It may be that the actual critical modes for the range of fields near the corner are different from those predicted from bulk instability theory. It is important to keep in mind that the bulk theory gives $k=0$ for these critical modes. In this limit, it is necessary to take the sample surface boundary conditions into account. This renders the spin wave instability analysis much more complicated, even for isotropic materials, and introduces magnetostatic mode considerations into the analysis.[43,44] This problem is still unresolved.

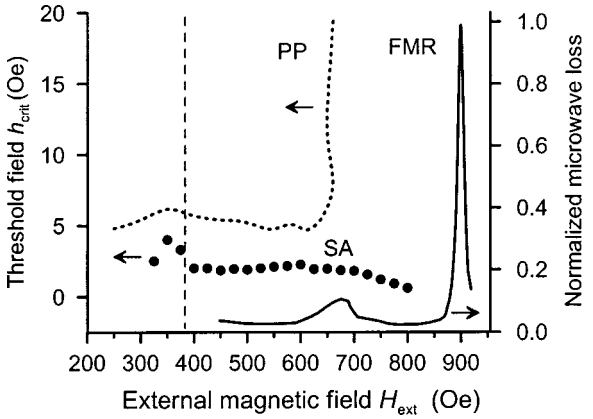

FIG. 11. Subsidiary absorption butterfly curve measurements on Zn–Y sample S3. The solid circles show the subsidiary absorption (SA) threshold field amplitude h_{crit} vs static external magnetic field H_{ext} data. The short dashed shows the parallel pump (PP) butterfly curve. The solid line shows the normalized ferromagnetic resonance (FMR) loss profile at low power. The vertical dashed line shows the field for magnetic saturation from Table I. The angle between the static magnetic field and the microwave field was set to 90°, 0°, and 8° for the SA, PP, and FMR measurements, respectively. The PP data are the same as shown in Fig. 9.

C. Subsidiary absorption

Figures 11 and 12 show results from the SA measurements and calculations. The figure formats follow those in

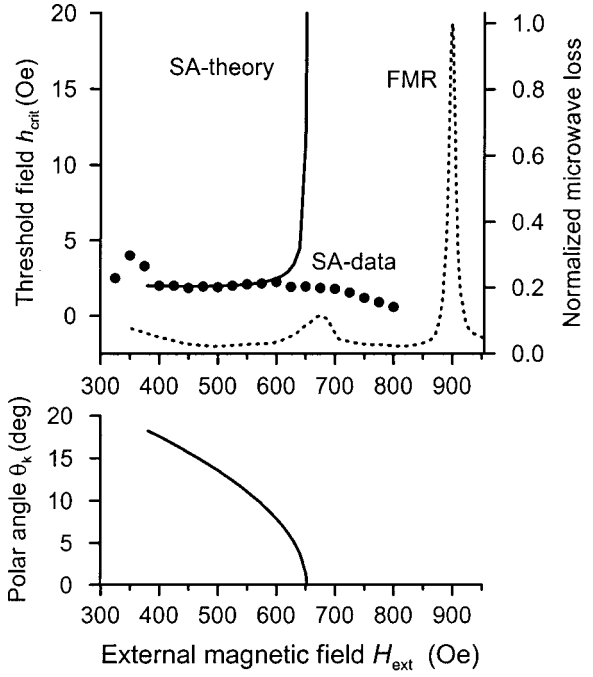

FIG. 12. Subsidiary absorption (SA) butterfly curve and critical mode results for sample S3. The upper graph shows the SA butterfly curve threshold field amplitude h_{crit} vs static external magnetic field H_{ext} data (solid circles) and fit (solid line). The dotted line is the low power FMR response. The lower graph shows the critical mode polar angle θ_k vs H_{ext}.

Downloaded 02 Apr 2001 to 129.82.192.18. Redistribution subject to AIP copyright, see http://ojps.aip.org/japo/japcr.jsp

Figs. 9 and 10. Only results for sample S3 are shown. As reference points for the discussion below, the dashed line butterfly curve in Fig. 11 shows the PP h_{crit} data from Fig. 9(c) and the solid line depicts the low power FMR absorption curve. The vertical dashed line in Fig. 11 indicates the static field required for magnetic saturation, H_{in}, from Table I. As before, all results are for a nominal operating frequency of 8.93 GHz. The subsidiary absorption data were obtained with the angle between the static and microwave fields, the θ parameter in Fig. 4, set at 90°. For the low power FMR loss profile, this angle was set at 8°. Note that the h_{crit} data in both figures extend to field values that are somewhat above the subsidiary loss and first order process cutoff point at $H_{ext}=H_{cut}=650$ Oe.

Figure 11 shows that the overall SA response for h_{crit} as a function of H_{ext} is very different from the parallel pump butterfly curve response. Three specific points of comparison may be noted. First, note that the SA h_{crit} response and the PP response show small maxima at about the same field. This field is slightly below the saturation field point at $H_{ext}=H_{in}=380$ Oe. Unfortunately, neither the SA or PP data were extended to zero field. In this limit, there should be no difference between parallel and transverse pumping and the h_{crit} values should converge.

The second point to note is the much lower values of the SA h_{crit}, relative to the thresholds for parallel pumping in the region between $H_{ext}=H_{sat}$ and $H_{ext}=H_{cut}$. The reduction in threshold relative to the PP h_{crit} values for these Zn–Y materials may be significant. For YIG materials, one always finds that the SA threshold at low field is above the PP threshold.[45,46] Here, the order appears to be reversed. Fits of the theory to the data and spin wave linewidth implications are considered below.

The third point to note is that the SA h_{crit} vs. H_{ext} response for a further increase in field does not follow the usual result for conventional low anisotropy or polycrystalline ferrite materials. For such samples, one usually finds a threshold which (i) first decreases with increasing field for a range of low fields for which the critical mode wave number is nonzero and then (ii) diverges as the external field approaches $H_{ext}=H_{cut}$. Neither of these standard subsidiary absorption responses is found here. The data in Fig. 11 show a range of fields from about 400 to 700 Oe for which the threshold is more or less constant. There is certainly no divergence in h_{crit} at $H_{ext}=H_{cut}=650$ Oe. Then, for fields above 700 Oe or so, there is a rapid decrease in h_{crit}. Except for the initial match with the parallel pump threshold at the lowest fields and the initial drop in h_{crit} as the field is increased, these data look nothing like the usual subsidiary absorption butterfly curves.

The different character for the subsidiary absorption response found for Zn–Y disks is related to two anisotropy effects. First, there is the spin wave band shift. The planar anisotropy shifts the spin wave band up by a significant amount. Second, there is the FMR shift. The anisotropy shifts the FMR and magnetostatic mode resonance fields down so that these resonances are close to or even inside the subsidiary absorption regime. These shifts have a major effect on the h_{crit} response.

The shape of the h_{crit} vs. H_{ext} response between 400 and 600 Oe is then due to a combination of factors. First, there is the θ_k dependence of the critical mode coupling factor $W_k^{(1)}$ for the zero k or close to zero k, critical modes. Second, there is the field dependence of the uniform mode and magnetostatic mode responses. As one moves up in field and down in θ_k for modes at $\omega_k=\omega_p/2$ and $k=0$, the coupling factor decreases. At the same time, one is moving up the tail of the magnetostatic and uniform mode response curve, as in Fig. 11, and this increases the net coupling to the SA modes. Model calculations in Fig. 12, to be considered shortly, indicate that the θ_k and FMR response factors combine to give a relatively field independent threshold in the 400–600 Oe field range. In principle, one should also include a possible **k**-dependent spin wave linewidth ΔH_k. As the Fig. 12 results will show, it is possible to fit the data with a constant ΔH_k.

The FMR and magnetostatic mode shifts to lower fields introduce additional complications. The low power FMR data in Fig. 11, for sample S3, show a prominent magnetostatic mode peak centered at about 675 Oe and the uniform mode peak at 900 Oe. For sample S3, these modes were far enough above H_{cut} to maintain a more or less flat h_{crit} vs. H_{ext} character for fields up to $H_{ext}=H_{cut}$. For samples S1 and S2, the FMR peak, and the below FMR magnetostatic mode resonances were too low in field to obtain any thresholds that could be uniquely associated with the usual subsidiary absorption.

Even for sample S3, however, the proximity of these resonances to H_{cut} was sufficient to suppress the usual SA threshold divergence at $H_{ext}=H_{cut}$. For fields above $H_{ext}=H_{cut}$, it appears that the onset of second order processes cause the h_{crit} response to go smoothly from the constant threshold found for first order processes to the rapid drop in threshold associated with the resonance saturation butterfly curve response discussed above. Note that the approach to FMR in Figs. 7 and 8 cause the measured second order h_{crit} to drop to values as low as a few tenths Oe. The SA data for fields above H_{cut} show this same trend. The drop in h_{crit} is not as sharp as one might extrapolate from the RS results in Figs. 7 and 8. This is probably due to the additional cavity loading effects which come in as one approaches the FMR field with the pump angle θ set at 90°.

Figure 12 shows the h_{crit} vs. H_{ext} data from Fig. 11 along with a computed subsidiary absorption butterfly curve and details on the critical mode θ_k versus field response associated with the computed thresholds. The critical mode k and ϕ_k values were 0° and 90°, respectively, over the entire subsidiary absorption region. The calculated butterfly curve and critical modes were obtained for the sample parameters indicated above and a constant spin wave linewidth value of 18 Oe. The low power FMR response profile is shown again as a point of reference.

As indicated in the discussion for Fig. 11, the flat portion of the theoretical butterfly curve response can be matched to the data for fields between 400 and 600 Oe. The various factors which yield a field dependent threshold for isotropic or low anisotropy cubic ferrites appear to combine to produce a relatively field independent h_{crit} for subsidiary absorp-

Downloaded 02 Apr 2001 to 129.82.192.18. Redistribution subject to AIP copyright, see http://ojps.aip.org/japo/japcr.jsp

tion in Zn–Y planar materials. It may be significant that the fit shown is obtained for a fixed value of the spin wave linewidth at $\Delta H_k = 18$ Oe, the same as used for the parallel pumping butterfly curve fit for sample S3. These consistent fits for PP and SA $h_{\rm crit}$ values which differ by a factor of two, and the relatively large value of ΔH_k needed for the fit, indicate (i) that the data and analysis are valid and consistent and (ii) that these single crystal Zn–Y materials are still far from perfect and the linewidths are far from intrinsic. This conclusion is also supported by the lack of any significant **k**-dependent linewidth term for the fits.

The divergence in the theoretical $h_{\rm crit}$ values as $H_{\rm ext}$ approaches $H_{\rm cut}$ is due to the band edge for available spin wave modes at $\omega_k = \omega_p/2$. The measured thresholds hold at a more or less fixed level in this regime due to the FMR and magnetostatic mode response and the coupling factors noted above.

The critical mode response is quite different from the behavior for parallel pumping. As the bottom part of Fig. 12 shows, one now has a drop in the polar spin wave angle θ_k with increasing field. As previously indicated, the relevant calculated critical modes also have $k=0$ and $\phi_k = 90°$. It is important to note the contrast between these critical modes and those for parallel pumping. In the PP case, one initially has nonzero k values which decrease as the field increases, a fixed θ_k at 90°, and $\phi_k = 0°$.

As emphasized above, the fact that one can fit the low field portions of the butterfly curves for these two very different processes with one and the same fixed 18 Oe value of ΔH_k provides a good indication that the spin wave linewidth for first order processes in these materials is **k** independent and that the analysis is self consistent. There is however, a clear problem between the PP and SA results and the RS fits. Recall that for resonance saturation, a k dependent spin wave linewidth was critical to the fits shown in Fig. 8. In the RS case, moreover, the nominal value of ΔH_k needed to fit the data was about 7 Oe for critical modes at the pump frequency. For the PP and SA cases, the critical modes are half the pump frequency and the fitted spin wave linewidth is a factor of 2–3 larger. Larger linewidths for a lower frequency indicate a very complex and possibly process dependent spin wave linewidth.

V. SUMMARY AND CONCLUSIONS

The RS, SA, and PP spin wave instability threshold measurements have been made on single crystal easy plane disks of Mn substituted Y type hexagonal ferrite materials at 8.93 GHz and room temperature. The RS results represent the first actual butterfly curve data for resonance saturation. The data indicate a **k**-dependent spin wave linewidth effect as one moves between thresholds close to and away from the FMR peak. The nominal spin wave linewidth needed to match the data was 7 Oe. The SA and the PP threshold fields were approximately constant at low field and rapidly increased at higher fields. The spin wave linewidth that best matched these results was **k** independent and equal to ~18 Oe.

These experimental and theoretical results raise important questions about the critical modes and spin wave linewidths in hexagonal ferrite materials. (1) They indicate that the true intrinsic loss limit has not yet been achieved. (2) They indicate that there are process dependent effects which control the **k**-dependent linewidth even in these nonintrinsic situations. (3) The theory indicates a possible parallel pump butterfly curve high field corner structure which is yet to be resolved clearly from experiment.

ACKNOWLEDGMENTS

This work was supported, in part, by the United States Office of Naval Research (ONR), Grant Nos. N00014-90-J-4078, N00014-94-1-0096, and N0014-95-1-1130. The sample was grown at Purdue University under ONR Grant No. N00014-91-J-1323. Dr. J. J. Green and Raytheon Company, Lexington, MA are gratefully acknowledged for a donation of microwave instrumentation for high power measurements. The authors are also grateful to R. E. Eykholt for helpful discussions of the theory, and to A. V. Nazarov for a detailed reading of the text. Part of the work by CEP was done on sabbatical at the Universität Kaiserslautern, Germany with support from the Alexander von Humboldt Foundation.

APPENDIX A

This appendix provides working equations for the first order spin wave instability coupling coefficient $W_k^{(1)}$ introduced in Sec. II. The $W_k^{(1)}$ coefficient may be written in the form

$$W_k^{(1)} = \frac{1}{\omega_m}(\omega_L q_L + \omega_{\rm AL} q_{\rm AL}^*), \tag{A1}$$

for transverse pumping and

$$W_k^{(1)} = \frac{c_Z}{\omega_m}, \tag{A2}$$

for parallel pumping. The $q_{\rm L}$ and $q_{\rm AL}$ parameters in Eq. (A1) denote the Larmor (L) and anti-Larmor (AL) components of the uniform mode response to the transverse microwave field. The $\omega_{\rm L}$ and $\omega_{\rm AL}$ coefficients represent coupling rates for energy from the uniform mode into a given spin wave mode at wave vector **k** and spin wave frequency $\omega_k = \omega_p/2$. The c_Z parameter in Eq. (A2) is the parallel pumping coupling coefficient.

The $q_{\rm L}$ and $q_{\rm AL}$ uniform mode response terms in Eq. (A1) may be evaluated for the y directed pump field used in the experiment from the usual torque equation with ''Gilbert'' damping.[47] These terms may be expressed in inverse frequency units and written as

$$q_{\rm L} = (\omega_a + \omega_p)\left(\frac{2\eta_{\rm FMR}\omega_p + i(\omega_{\rm FMR}^2 - \omega_p^2)}{(2\eta_{\rm FMR}\omega_p)^2 + (\omega_{\rm FMR}^2 - \omega_p^2)^2}\right), \tag{A3}$$

and

$$q_{\rm AL} = (\omega_a - \omega_p)\left(\frac{-2\eta_{\rm FMR}\omega_p + i(\omega_{\rm FMR}^2 - \omega_p^2)}{(2\eta_{\rm FMR}\omega_p)^2 + (\omega_{\rm FMR}^2 - \omega_p^2)^2}\right). \tag{A4}$$

Downloaded 02 Apr 2001 to 129.82.192.18. Redistribution subject to AIP copyright, see http://ojps.aip.org/japo/japcr.jsp

In the above, $\omega_a = |\gamma| H_a$ denotes an effective stiffness frequency related to the stiffness field H_a given in Eq. (7) for a tipping of the magnetization out of the disk plane and η_{FMR} is the uniform mode relaxation rate.

It is important to note that the effect of loss is included explicitly in the q_{L} and q_{AL} terms given above. Most treatments of subsidiary absorption first order processes do not include loss in the uniform mode response because the FMR field is usually well above the subsidiary loss field regime. In the present case, the FMR response is rather close to the subsidiary loss regime and it is important to include the full response with damping. The η_{FMR} term is the relaxation rate of the uniform mode expressed in frequency units. In general, η_{FMR} is directly related to the FMR linewidth (ΔH_{FMR}) for resonance at a fixed field. As such, η_{FMR} is connected to ΔH_{FMR} according to the condition

$$\eta_{\mathrm{FMR}} = \Delta H_{\mathrm{FMR}} \left(\frac{\partial \omega_{\mathrm{FMR}}}{\partial H_{\mathrm{ext}}} \right)_{H_{\mathrm{ext}} = H_{\mathrm{FMR}}}. \tag{A5}$$

For the FMR configuration used here, this expression reduces to

$$\eta_{\mathrm{FMR}} = \frac{|\gamma|^2}{4} \left(\frac{H_a + H_b}{\omega_{\mathrm{FMR}}} \right) \Delta H_{\mathrm{FMR}}, \tag{A6}$$

where H_a and H_b are the FMR stiffness fields introduced in Sec. II. The ω_{L} and ω_{AL} coupling terms in the $W_k^{(1)}$ expression for transverse pumping constitute the key results for the first order theory. These coupling terms are somewhat complicated for isotropic materials[18] and are even more complicated when anisotropy is included.[17] For planar hexagonal ferrites, the first order analysis gives ω_{L} and ω_{AL} expressions which may be written as

$$\omega_{\mathrm{L}} = (A_k' + \omega_k) g_k e^{-2i\phi_A} - B_k' g_k^*, \tag{A7}$$

and

$$\omega_{\mathrm{AL}} = (A_k' - \omega_k) g_k^* e^{+2i\phi_A} - B_k' g_k. \tag{A8}$$

The A_k' and B_k' in Eqs. (A7) and (A8) may be written in terms of the corresponding A_k and B_k parameters in Ref. 18:

$$A_k' = A_k + \frac{|\gamma| H_A}{2}, \tag{A9}$$

$$B_k' = \sqrt{(B_k \cos 2\phi_k + \tfrac{1}{2}|\gamma| H_A)^2 + B_k^2 \sin^2 2\phi_k}. \tag{A10}$$

The A_k and B_k are given by

$$A_k = |\gamma| H_{\mathrm{int}} + \tfrac{1}{2} \omega_m \sin^2 \theta_k + |\gamma| D k^2 \tag{A11}$$

and

$$B_k = \tfrac{1}{2} \omega_m \sin^2 \theta_k. \tag{A12}$$

The g_k parameter in Eqs. (A7) and (A8) may be written as

$$g_k = \omega_m \cos \theta_k \sin \theta_k e^{+i\phi_k}, \tag{A13}$$

where θ_k and ϕ_k are the polar and azimuthal spin wave propagation angles defined in Sec. II. Finally, the ϕ_A angle parameter is related to ϕ_k according to

$$\phi_A = \frac{1}{2} \tan^{-1} \left(\frac{B_k \sin 2\phi_k}{B_k \cos 2\phi_k + \tfrac{1}{2}|\gamma| H_A} \right). \tag{A14}$$

The above series of equations apply to the $W_k^{(1)}$ coupling coefficient for subsidiary absorption in Eq. (A1). These formulas apply when the microwave field is transverse to the static field and in the plane of the disk. In the case of parallel pumping with the static and microwave fields in plane Eq. (A2) applies. The c_Z parameter in Eq. (A2) is given by

$$c_Z = 2 B_k'. \tag{A15}$$

APPENDIX B

This appendix provides working equations for the second order spin wave instability coupling coefficient $W_k^{(2)}$ introduced in Sec. II. This coefficient may be written in the form

$$W_k^{(2)} = C[\omega_\lambda^2 q_L^2 + \omega_\alpha^2 (q_{\mathrm{AL}}^*)^2 + \omega_{\lambda\alpha}^2 q_{\mathrm{L}} q_{\mathrm{AL}}^*]. \tag{B1}$$

The C term in Eq. (B1) may be written as

$$C = \frac{(|\gamma| \Delta H_{\mathrm{FMR}})^2}{4 \omega_k \omega_m}. \tag{B2}$$

The ω_λ^2, ω_α^2, and $\omega_{\lambda\alpha}^2$ factors represent second order coupling terms for the indicated uniform mode response components and energy flow into spin wave modes at $\omega_k = \omega_p$. These coupling terms may be written as

$$\omega_\lambda^2 = (A_k' + \omega_k) l_k e^{-2i\phi_A} - B_k' p_k. \tag{B3}$$

$$\omega_\alpha^2 = (A_k' - \omega_k) l_k e^{+2i\phi_A} - B_k' p_k. \tag{B4}$$

and

$$\omega_{\lambda\alpha}^2 = (A_k' + \omega_k) r_k e^{-2i\phi_A} + (A_k' - \omega_k) r_k^* e^{+2i\phi_A} - B_k' s_k. \tag{B5}$$

The A_k, ω_k, ϕ_A, and B_k' terms are given in Appendix A. The l_k, p_k, r_k, and s_k factors are given by

$$l_k = \frac{|\gamma| D k^2}{2} + \frac{\omega_m}{2} \cos^2 \theta_k - \frac{|\gamma| H_A}{4} - \frac{\omega_m}{4} (N_x + N_z), \tag{B6}$$

$$p_k = -\frac{|\gamma| H_A}{4} - \frac{\omega_m}{4} (N_x - N_z), \tag{B7}$$

$$r_k = -\frac{B_k}{2} e^{+2i\phi_k} - \frac{|\gamma| H_A}{2} - \frac{\omega_m}{4} (N_x - N_z), \tag{B8}$$

and

$$s_k = -|\gamma| H_A + \frac{\omega_m}{2} (-N_x + N_z + 3 \cos^2 \theta_k - 1). \tag{B9}$$

[1] C. E. Patton, IEEE Trans. Magn. **24**, 2024 (1988).
[2] C. Vittoria, J. Magn. Magn. Mater. **21**, 109 (1980).
[3] G. P. Rodrigue, IEEE Trans. Microwave Theory Tech. **MTT-11**, 351 (1963).
[4] M. A. Wittenauer, J. A. Nyenhuis, A. I. Schindler, H. Sato, F. J. Friedlaender, J. Truedson, R. Karim, and C. E. Patton, J. Cryst. Growth **130**, 533 (1993).
[5] R. O. Savage and A. Tauber, J. Am. Ceram. Soc. **47**, 13 (1964).
[6] G. P. Rodrigue, Adv. Ceram. **21**, 37 (1985).

Downloaded 02 Apr 2001 to 129.82.192.18. Redistribution subject to AIP copyright, see http://ojps.aip.org/japo/japcr.jsp

[7] S. B. Thompson and G. P. Rodrigue, IEEE Trans. Microwave Theory Tech. **MTT-33**, 1204 (1985).
[8] J. R. Truedson, P. Kabos, K. D. McKinstry, and C. E. Patton, J. Appl. Phys. **76**, 432 (1994).
[9] M. J. Hurben, D. R. Franklin, and C. E. Patton, J. Appl. Phys. **81**, 7458 (1997).
[10] U. Milano and E. Schlömann, *Spin-wave Instabilities in a Microwave Magnetic Field Applied Parallel to the dc Field*, IEEE Proc. 109b, suppl. 21 (1962) pp. 59–65.
[11] H. Suhl, J. Phys. Chem. Solids **1**, 209 (1957).
[12] E. Schlömann, J. J. Green, and U. Milano, J. Appl. Phys. **31**, 386S (1960).
[13] R. W. Damon, Rev. Mod. Phys. **25**, 239 (1951).
[14] N. Bloembergen and S. Wang, Phys. Rev. **93**, 72 (1954).
[15] E. Schlömann, Technical Report No. R-48, Raytheon Co., 1959 (unpublished).
[16] E. Schlömann, R. I. Joseph, and I. Bady, J. Appl. Phys. **34**, 672 (1963).
[17] C. E. Patton, Phys. Status Solidi B **92**, 211 (1979).
[18] C. E. Patton, J. Appl. Phys. **40**, 2837 (1969).
[19] M. Chen and C. E. Patton, *Nonlinear Phenomena and Chaos in Magnetic Materials*, edited by P. E. Wigen (World Scientific, Singapore, 1994), Chap. 3.
[20] J. A. Osborn, Phys. Rev. **67**, 351 (1945).
[21] C. Kittel, Phys. Rev. **71**, 270 (1947).
[22] C. Herring and C. Kittel, Phys. Rev. **81**, 869 (1951).
[23] M. Mita and H. Shinizu, J. Phys. Soc. Jpn. **35**, 414 (1973).
[24] M. J. Hurben and C. E. Patton, J. Appl. Phys. **83**, 4344 (1988).
[25] A. Tauber, S. Dixon, and R. O. Savage, J. Appl. Phys. **35**, 1008 (1964).
[26] R. O. Savage, S. Dixon, and A. Tauber, J. Appl. Phys. **36**, 873 (1965).
[27] Y. T. Zhang, C. E. Patton, G. Srinivasan, G. O. White, C. J. Brower, and C. A. Edmondson, Rev. Sci. Instrum. **58**, 620 (1987).
[28] K. D. McKinstry and C. E. Patton, Rev. Sci. Instrum. **60**, 439 (1989).
[29] K. D. McKinstry, C. E. Patton, and M. Kogekar, J. Appl. Phys. **58**, 925 (1985).
[30] C. E. Patton and J. J. Green, Rev. Sci. Instrum. **42**, 193 (1971).
[31] J. J. Green and T. Kohane, *Testing of Ferrite Materials for Microwave Applications*, Semiconductor Products and Solid State Technology, Vol. 7 (1964) pp. 46–52.
[32] Y. H. Yiu and C. E. Patton, J. Appl. Phys. **53**, 5116 (1982).
[33] P. Kabos, C. E. Patton, G. Wiese, A. D. Sullins, E. S. Wright, and L. Chen, J. Appl. Phys. **80**, 3962 (1996).
[34] J. J. Green and B. J. Healy, J. Appl. Phys. **34**, 1285 (1963).
[35] J. Helszajn and J. McStay, IEEE Trans. Microwave Theory Tech. **MTT-18**, 518 (1970).
[36] A. G. Gurevich, A. V. Nazarov, and O. A. Chivileva, Phys. Solid State **41**, 1513 (1999).
[37] A. Tauber (private communication).
[38] C. E. Patton, IEEE Trans. Magn. **MAG-8**, 433 (1972).
[39] G. O. White and C. E. Patton, J. Magn. Magn. Mater. **9**, 299 (1978).
[40] T. M. Robinson, J. Appl. Phys. **72**, 607 (1992).
[41] Y. H. Liu and C. E. Patton, J. Appl. Phys. **53**, 5116 (1981).
[42] R. Karim, S. D. Ball, J. R. Truedson, and C. E. Patton, J. Appl. Phys. **73**, 4512 (1993).
[43] M. Chen and C. E. Patton, J. Appl. Phys. **69**, 5724 (1991).
[44] D. N. Chartaryzhskii, B. A. Kalinikos, and O. G. Vendik, Solid State Commun. **20**, 985 (1976).
[45] C. E. Patton, *Ferrites: Proceedings of the International Conference* (University of Tokyo Press, Tokyo, 1980), p. 807.
[46] L. M. Silber and C. E. Patton, IEEE Trans. Magn. **MAG-18**, 1630 (1982).
[47] M. Laksmanan and K. Nakamura, Phys. Rev. Lett. **53**, 2497 (1984).

Downloaded 02 Apr 2001 to 129.82.192.18. Redistribution subject to AIP copyright, see http://ojps.aip.org/japo/japcr.jsp